



UNIVERSITY OF GRONINGEN

PHYSICS

BACHELOR RESEARCH PROJECT

Measurement of the Raw Asymmetry Ratio in the Decay $\Lambda_b^0 \rightarrow \Lambda^0 (\rightarrow p\pi^-) J/\psi (\rightarrow e^+e^-)$

Author:

Ludovica DE MARE
S4966996

First supervisor:

Ann-Kathrin PERREVOORT

Second supervisor:

Steven HOEKSTRA

October 15, 2024

Abstract

It is essential to confirm that no CP violation (CPV) is observed in the $\Lambda_b^0 \rightarrow \Lambda^0 (\rightarrow p\pi^-) J/\psi (\rightarrow e^+e^-)$ decay in order to use it as a normalization channel for testing CPV in the $\Lambda_b^0 \rightarrow e^+e^-\Lambda^0$ decay. In this thesis, an analysis is conducted on LHC Run 2 data (years 2016–2018), corresponding to an integrated luminosity of 5.57 fb^{-1} , collected by the LHCb experiment from proton-proton collisions at $\sqrt{s} = 13 \text{ TeV}$. From the data, events compatible with the signal decay are selected and a suppression of the background process $B^0 \rightarrow J/\psi K_s^0$ based on kinematic properties is applied. In order to test for detection asymmetries, events taken at the two different polarities of the LHCb dipole magnet are analyzed, separately. Signal yields of Λ_b^0 and $\bar{\Lambda}_b^0$ along with the raw asymmetry ratio, are extracted through binned fits for each sample and the combined dataset. No detection asymmetry is observed and a raw asymmetry ratio of $A_{raw} = 0.029 \pm 0.032$ is measured for the combined dataset, leading to the conclusion that, in this study, no CP violation is observed in the decay.

Acknowledgements

I would like to thank my supervisor Ann-Kathrin Perrevoort for guiding me through these three months of thesis and being always available for help and clarifying my doubts.

I would also like to thank the LHCb group for being so welcoming and for the nice lunch breaks.

This summer thesis could have been more challenging without a nice group of people around.

I would also like to thank all my friends, without you these three years would have been probably more difficult and for sure way more boring.

Finally, I would like to give a special thanks to my family for always supporting me and believing in me.

Contents

1 Motivation	4
2 Theory	5
2.1 The Standard Model	5
2.2 The LHCb detector	6
2.3 $\Lambda_b^0 \rightarrow \Lambda^0 J/\psi$ decay	8
2.4 Invariant mass	10
3 Methods	12
3.1 Λ_b^0 candidate selection	12
3.2 Λ_b^0 cut veto	12
4 Results	15
5 Discussion	18
6 Conclusion	19
7 References	20
8 Appendix	21

1 Motivation

The Standard Model (SM) is the most successful quantum field theory we have in describing the laws that govern matter and its interactions at a fundamental level. However, this theory results incomplete since it fails in describing phenomena such as dark matter, the excess in the abundance of matter over antimatter in the universe or gravity.

In particular, the surplus in the abundance of matter over antimatter, also called matter–antimatter asymmetry, is a concept closely related to Charge-Parity Violation (CPV).

In particle physics, Charge-Parity (CP) conservation is the combined operation of Charge conjugation and Parity. Charge conjugation is conserved when an interaction between particles is invariant under the exchange of each particle with its antiparticle while Parity is conserved when a physical process and its mirror image have the same probability to happen in nature. Hence, a transformation in which CP symmetry is conserved swaps a particle with the mirror image of its antimatter particle, which is identical but has opposite quantum numbers.

Thus, the physical laws that govern nature cannot conserve CP symmetry entirely. If they did, the universe would contain an equal amount of particles and antiparticles which would have annihilated each other, leaving behind a universe filled mostly with radiation.

Within the Standard Model CP violation is observed in the weak interaction of particles such as K^0 , B^0 and D^0 mesons [1]–[3], with the latter observation being the first evidence of this asymmetry for the charm quark.

However, the CPV observed within the SM is not sufficient to explain the present-day matter–antimatter imbalance. For this reason, LHCb experiment at CERN is dedicated to high precision measurements of CP violation on rare b hadron decays, where, if an asymmetry were observed, it could potentially point to physics Beyond the Standard Model (BSM).

In this analysis, CP violation is investigated on the $\Lambda_b^0 \rightarrow J/\psi \Lambda^0$ decay, where $J/\psi \rightarrow e^+e^-$.

This decay mode is particularly interesting because it is a good candidate for a normalization channel in testing CPV on the $\Lambda_b^0 \rightarrow e^+e^-\Lambda^0$ decay, in order to exclude the possibility that the eventual asymmetry observed is due to systematic errors. Indeed, both decays share the same final dielectron state while the $\Lambda_b^0 \rightarrow J/\psi \Lambda^0$ decay is more frequent than $\Lambda_b^0 \rightarrow e^+e^-\Lambda^0$.

The $\Lambda_b^0 \rightarrow J/\psi \Lambda^0$ decay treated in this analysis is particularly important also in the research for Lepton Flavour Universality (LFU) violation. LFU is a property emerging from the SM stating that up to mass correction all electroweak couplings of leptons to gauge bosons are independent of their flavour. In simpler words, we would for example expect electrons and muons to be produced in same amounts by electroweak decay (up to mass correction).

However, discrepancies between electron and muon decay channels such as $B^+ \rightarrow K^+ l^+ l^-$ [4], with $l = e, \mu$ suggest that decays involving electrons might be occurring at different rates than expected when compared to decays involving muons. In this context, a difference in the raw asymmetry ratio of Λ_b^0 and Λ_b^0 between electron $J/\psi \rightarrow e^+e^-$ and muon $J/\psi \rightarrow \mu^+\mu^-$ channels could provide further clues to the nature of LFU violations.

2 Theory

2.1 The Standard Model

The Standard Model (SM) shown in Figure 1 is the theoretical framework that best describes our current understanding of matter and its interactions at a fundamental level. According to this model, matter is made by fermions: particles with half-integer spin that follow Pauli exclusion principle, i.e. no two fermions can occupy the same quantum state simultaneously. Fermions are classified into quarks and leptons which interact through four fundamental forces: gravity, strong force, weak force and electromagnetic force. Only the latter three are described as gauge fields within the SM. They are mediated, respectively, by gluon g , W^\pm and Z^0 , photon γ . These particles form the family of gauge bosons together with the Higgs boson H which was discovered in 2012 and which gives mass to quarks, leptons, Z^0 and W^\pm particles [5], [6]. Gauge bosons have integer spin and can occupy the same quantum state simultaneously.

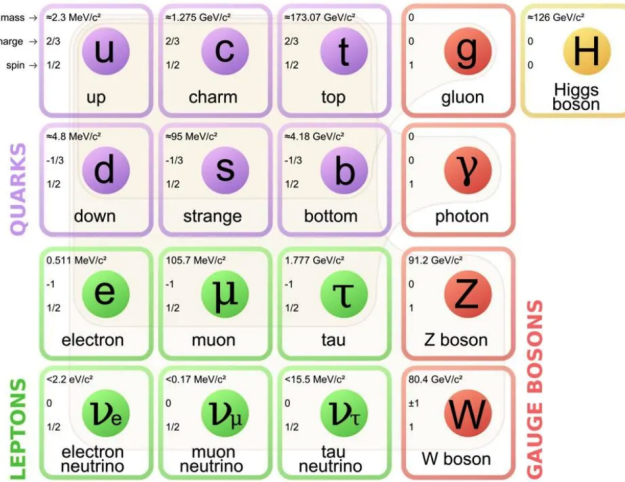


Figure 1: Overview of particles and their properties in the SM of particle physics [7].

Quarks and leptons come both in six different types, or flavours, and into three generations:

$$\begin{pmatrix} u \\ d \end{pmatrix}, \begin{pmatrix} c \\ s \end{pmatrix}, \begin{pmatrix} t \\ b \end{pmatrix}$$

$$\begin{pmatrix} \nu_e \\ e^- \end{pmatrix}, \begin{pmatrix} \nu_\mu \\ \mu^- \end{pmatrix}, \begin{pmatrix} \nu_\tau \\ \tau^- \end{pmatrix}$$

where each subsequent generation contains a particle that is similar but more massive than the previous one.

All six quarks and six leptons have their antiparticle with the same mass but opposite quantum numbers and, except neutrinos, opposite charge, resulting in 24 fundamental fermions.

The strong force acts exclusively between quarks, binding them together to form hadrons, which are categorized into two groups: baryons and mesons. Baryons consist of three quarks, such as the Λ_b^0 baryon, composed of up (u), down (d) and bottom (b) quarks. Mesons, on the other hand, are made of a quark-antiquark pair, such as the J/ψ meson, composed of a charm

quark (c) and a charm-antiquark (\bar{c}).

There are eight types of gluons in nature, each mediating the strong force and carrying a combination of color charges, a fundamental property also carried by quarks. The strong force is described by Quantum Chromodynamics (QCD).

The electromagnetic force interacts exclusively with charged particles, such as quarks, electrons, muons, and tau particles, and it is described by the framework of Quantum Electrodynamics (QED).

The weak force governs quark decay and is the only interaction that can change the flavour of a quark into another also between different generations [8]. This latter effect is taken into account in the SM by the elements of the unitary 3×3 Cabibbo-Kobayashi-Maskawa (CKM) matrix. The couplings from the CKM matrix favor transitions between up-type and down-type quarks from the same generation, but highly suppress transitions between quarks of different generations making them very rare to observe in nature. The complex phase of the matrix, instead, accounts for the CP violation observed in the weak interaction.

Also leptons interact via the weak force, however, couplings between leptons of different flavors were not originally allowed in the SM. This principle is known as lepton flavor conservation and for charged leptons, Lepton Flavor violations have not yet been observed. However, in the case of neutrinos it is observed that they oscillate and change flavour. This process can only occur if neutrinos have mass and it is described by the Pontecorvo-Maki-Nakagawa-Sakata (PMNS) matrix.

Finally, an important property of the electro-weak interaction is Lepton Flavour Universality (LFU) meaning that up to mass difference the coupling of leptons to the force mediators is the same, resulting in the same probability of these coupling to happen.

2.2 The LHCb detector

The LHCb experiment is dedicated to high precision measurements of CP violation and rare decays of b hadrons at the Large Hadron Collider (LHC) at CERN (Geneva). LHCb is a single-arm spectrometer, covering the pseudo-rapidity range $2 < \eta < 5$, which corresponds to particles that are emitted at very small angles with respect to the beam direction, equivalent to 15-250 mrad. The choice of the detector geometry is justified by the fact that at high energies, both the b and \bar{b} hadrons, are predominantly produced in the same forward or backward cone [9]. The layout of the LHCb spectrometer is shown in Figure 2. It consists of 4 sub-detectors: the tracking system, the calorimeter system, the RICH detectors and the muon system. The tracking system is composed of the Vertex Locator (VELO), four tracking stations TT, T1, T2, T3 and a magnet with a magnetic field strength of 4 Tm. The VELO is a silicon strip detector placed at 8 mm from the primary vertex (PV) which is where the proton-proton interaction occurs. The magnet is used to bend the trajectories of the particles allowing the measurement of their momenta, while its polarity is periodically reversed to mitigate systematic uncertainties caused by detection asymmetries. As a result, the recorded data is divided into two categories: Magnet Up (MU) and Magnet Down (MD) samples.

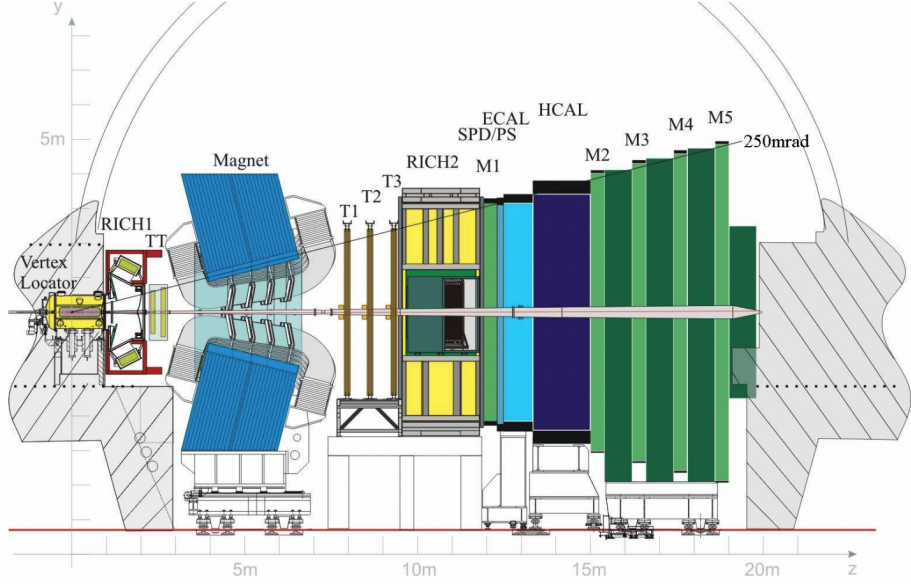


Figure 2: View of the LHCb detector [9].

The two Ring Imaging Cherenkov (RICH) detectors are responsible for the particle identification (PID) at the LHCb experiment. The detection principle is based on the Cherenkov radiation emitted by a charged particle travelling in a medium faster than the speed of light in that medium. The Cherenkov light is emitted at an angle with respect to the particle trajectory, which is directly related to the speed of the particle and the refractive index of the medium. The calorimeter system of LHCb consists of the Scintillating Pad Detector (SPD), the Pre-Shower Detector (PS), the Electromagnetic Calorimeter (ECAL) and the Hadronic Calorimeter (HCAL). The ECAL mainly distinguishes between electron and photons and measures the energy deposition of particles that interact via electromagnetic interaction and of neutral and charged hadrons. It is followed by the muon system which consists of five plane stations (M1-M5) which are used to identify and measure the tracks of muons.

Finally, it is useful to define the different track categories at LHCb shown in Figure 3. The tracks are defined into: VELO tracks, upstream tracks, long tracks (LL) and downstream tracks (DD). The first two categories correspond to particles with the shortest lifetimes. VELO tracks consist of hits only in the VELO, as seen with particles like Λ_b^0 , while upstream tracks have hits in both the VELO and TT stations. The long track category includes hits in the VELO, TT, and T stations, whereas particles with longer lifetimes such as Λ^0 , which can decay also after the VELO and leave hits only in the TT and T stations, correspond to downstream tracks.

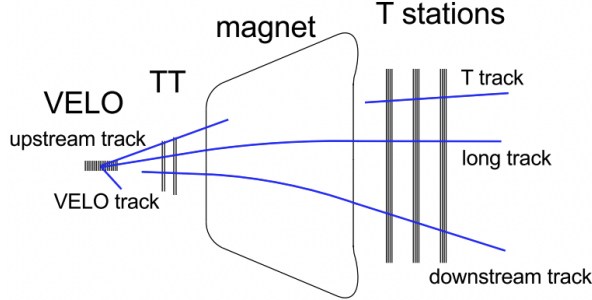


Figure 3: Different track types on the LHCb detector [10].

The CERN Large Hadron Collider was built to collide 7 TeV protons or heavy ions of equivalent rigidity [11]. The first proton run, between 2010 and 2013, was carried out at a center-of-mass energy of the proton-proton collisions of $\sqrt{s} = 3.5 - 4$ TeV. Run 1 resulted in important physics results, most notably the discovery of the Higgs boson by the ATLAS and CMS experiments [5], [6]. For Run 2, the second data taking period, between 2015 and 2018, several upgrades were done and the total energy of proton collisions was increased to $\sqrt{s} = 13$ TeV. In this analysis, data collected by the LHCb experiment from LHC Run 2 is used. The corresponding integrated luminosity, i.e. number of proton collisions per unit time per unit area, of each year of Run 2 is shown in the table below:

Year	2015	2016	2017	2018
Integrated Luminosity $\int \mathcal{L} (\text{fb}^{-1})$	0.33	1.67	1.71	2.19

Table 1: Integrated Luminosity data over the years of Run 2 [12].

After 2015, the trigger menu of LHCb was changed, and since 2015 is a small data set compared to the following years, it was not included in this analysis. The total luminosity of 2016-2018 data sets is indeed 5.57 fb^{-1} compared to 5.9 fb^{-1} of all 4 years.

2.3 $\Lambda_b^0 \rightarrow \Lambda^0 J/\psi$ decay

The decay studied in this research project is the $\Lambda_b^0 \rightarrow \Lambda^0 J/\psi$ process where $\Lambda^0 \rightarrow p\pi^-$ and $J/\psi \rightarrow e^-e^+$ as illustrated in the decay tree in Figure 4. The $\overline{\Lambda_b^0}$ version of the decay is shown in parentheses, where the J/ψ branch remains unchanged, since the J/ψ is its own antiparticle. The proton-proton collision occurs at the primary vertex (PV), where Λ_b^0 and $\overline{\Lambda_b^0}$ particles are produced. The decay tree is reconstructed from the final state particles to the initial state: when the LHCb detects a proton and a negatively charged pion, their combined invariant mass corresponds to the mass of a Λ^0 particle. Similarly, if an antiproton and a positively charged pion are detected, their invariant mass reconstructs the $\overline{\Lambda_b^0}$ particle. Particles and antiparticles have same mass, hence they are distinguished by the detector by charge.

A similar procedure is applied to reconstruct the invariant mass of the Λ_b^0 from its subdecays.

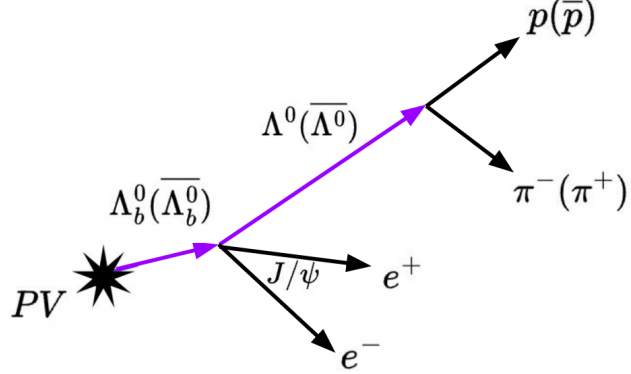


Figure 4: The decay tree of $\Lambda_b^0 \rightarrow \Lambda^0 J/\psi$ ($\bar{\Lambda}_b^0 \rightarrow \bar{\Lambda}^0 J/\psi$).

The length of the arrows in Figure 4 is proportional to the lifetime of the particles: the Λ^0 particle has the longest lifetime and it can decay inside or outside the VELO, while the Λ_b^0 baryon has a shorter lifetime and it always decays inside the VELO region. The J/ψ particle, instead, is so short lived that it is not detected by LHCb and its mass is completely reconstructed from the dielectron pair.

The mean lifetime literature values of these particles are shown in the table below[13]:

	τ (s)
J/ψ	$(7.11 \pm 0.13) \times 10^{-21}$
Λ_0	$(2.617 \pm 0.010) \times 10^{-10}$
Λ_b^0	$(1.462 \pm 0.014) \times 10^{-12}$

Table 2: Mean lifetime literature values.

Moreover, the decay process is represented by a Feynman diagram illustrated in Figure 5. The diagram shows the decay of Λ_b^0 baryon into a J/ψ meson and a Λ^0 baryon via a weak interaction mediated by a W^- boson. In this decay, the bottom quark (b) in the Λ_b^0 baryon undergoes a week decay into a charm quark (c) and a W^- boson. The W^- boson then decays into an anti-charm quark (\bar{c}) and a strange quark (s), which results in the formation of the J/ψ meson and the Λ^0 baryon. This process involves both the weak and strong interactions. The weak interaction governs the decay of the heavy b-quark, while the strong interaction is responsible for binding quarks to form the final-state hadrons.

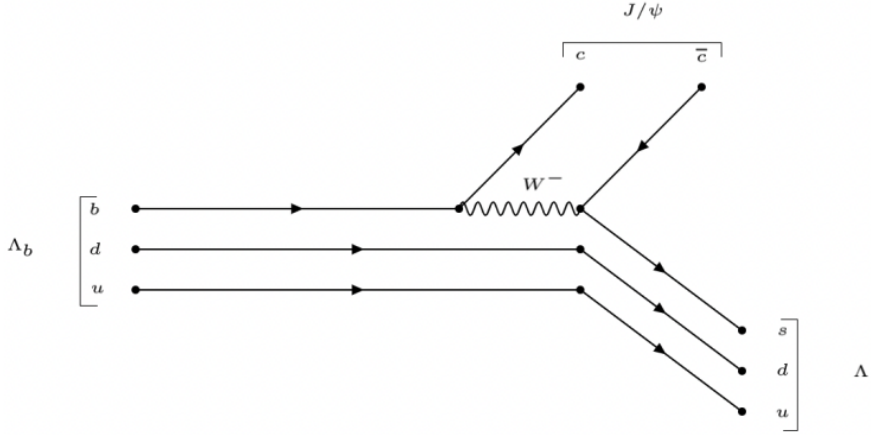


Figure 5: Tree level $\Lambda_b^0 \rightarrow J/\psi \Lambda^0$ Feynman diagram [14].

Particle decays that are described by a tree level Feynman diagram are not expected to show matter-antimatter asymmetry. Decay events described by higher order Feynman diagrams, instead, such as penguin or box diagrams, as non-SM particles may also contribute to the decay amplitudes, can be used to search for physics beyond the SM [15].

2.4 Invariant mass

Invariant mass or rest mass relates the energy and momentum to the mass of a system which is independent of the reference frame. The detector measures the total energy and momentum of the particle decay products at the decay vertex and reconstructs the mass of the particle. Equation 1 shows the invariant mass of dielectron pair from which J/ψ particle mass is reconstructed:

$$m_{ee} = \sqrt{(E_{e^-} + E_{e^+})^2 - (\vec{p}_{e^-} + \vec{p}_{e^+})^2} \quad (1)$$

while Equation 2 shows how it is obtained the invariant mass of the Λ^0 particle from its decay products:

$$m_{\Lambda^0} = \sqrt{(E_\pi + \sqrt{m_p^2 + p_p^2})^2 - (\vec{p}_p + \vec{p}_\pi)^2} \quad (2)$$

It follows that the mass probability distributions of the J/ψ , Λ^0 and Λ_b^0 particles are obtained, each showing a peak corresponding to the literature value of their respective mass. The mass literature values of the particles involved in the studied decay are shown in the table below [13]:

	m (MeV)
p	$938.27208816 \pm 0.00000029$
π	139.57039 ± 0.00018
e	$0.51099895000 \pm 0.00000000015$
Λ^0	1115.683 ± 0.006
J/ψ	3096.900 ± 0.006
Λ_b^0	5619.60 ± 0.17

Table 3: Mass literature values.

3 Methods

3.1 Λ_b^0 candidate selection

A signal $\Lambda_b^0 \rightarrow J/\psi\Lambda$ decay candidate is reconstructed from a Λ^0 baryon and a J/ψ meson candidate. A signal candidate selection is applied on the data in order to distinguish this decay mode from other b-hadron decays with comparable final state products. In particular, only dielectron invariant mass squared q^2 compatible with a $J/\psi \rightarrow e^+e^-$ decay is considered i.e. $6 < q^2 < 11 \text{ MeV}^2$ [16].

3.2 Λ_b^0 cut veto

The Run 2 dataset from 2016–2018 is divided into two categories: long tracks (LL) and downstream tracks (DD), with each category further split into magnet up (MU) and magnet down (MD) data samples.

In this section Λ_b^0 cut veto analysis is conducted uniquely on DDMD data and the cut range found is applied to all data sets. Although the background shape is observed to be different, especially between LL and DD data, it is assumed that for the scope of this thesis, conducting the analysis for each different set, was not leading to a better final result or smaller uncertainty. Moreover, the DD data set has worse resolution than LL one, hence, starting with it to analyse the cut veto is considered the best choice.

Monte Carlo (MC) simulation is used to predict and check consistency of methods and results on data. MC simulation models background due to other decay modes and detector misidentification. In this analysis MC was used to study the $B^0 \rightarrow J/\psi K_s^0$ background decay with $K_s^0 \rightarrow \pi^+\pi^-$, where one of the pions is misidentified as a proton [15]. In order to distinguish among Λ^0 signal and K_s^0 background Equation 2 is used replacing the proton mass with the mass of the pion. By applying the modified version of the equation to the data the reconstructed K_s^0 mass distribution shown in Figure 6 is obtained, where the peak corresponds to the K_s^0 background, while the area around it to the signal.

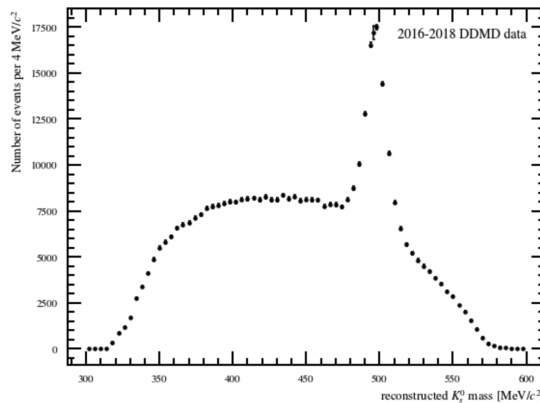


Figure 6: Reconstructed K_s^0 mass on DDMD data.

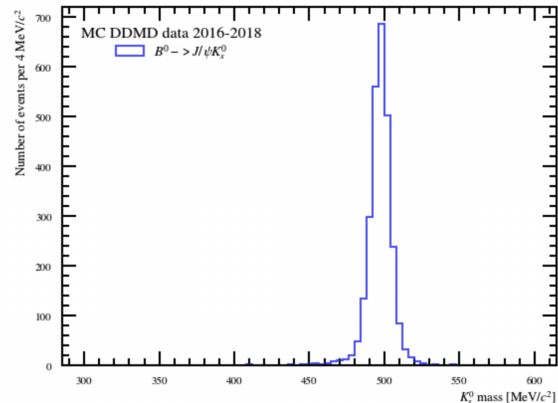


Figure 7: Simulated K_s^0 mass distribution on DDMD, MC data.

Different mass ranges are built using the reconstructed K_s^0 mass of simulated $B^0 \rightarrow J/\psi K_s^0$ events shown in Figure 7. The mean of this distribution, $\bar{m}_{K_s^0}^{rec} = 497 \text{ MeV}$ is used as the center

of symmetry and the standard deviation, $\sigma(m_{K_s^0}^{rec}) = 6.5$ MeV, to construct the widths of the ranges. As a result 40 ranges are defined in multiples of $\pm \frac{1}{3}$ of σ , or 2.2 MeV, around the mean of 497 MeV. Signal efficiency and background acceptance are calculated for each interval and displayed in Figure 8.

The range that maximally reduces the background and minimally affects the signal was chosen by calculating the gradient of the curve. A slope value less than 1 means that increasing the background acceptance leads to diminishing returns in terms of signal efficiency. Large veto ranges are found in the left part of the graph where the curve has a gradient larger than 1, whereas small veto ranges are found on the right side where the gradient is below 1. The gradient is calculated for the intermediate values to find the point where the increase in signal efficiency becomes smaller compared to the increase in background acceptance. This point is marked in red on the curve, which corresponds to a veto range of [483.8, 510.2] MeV, to a signal efficiency of 85% and to a background acceptance of 8%.

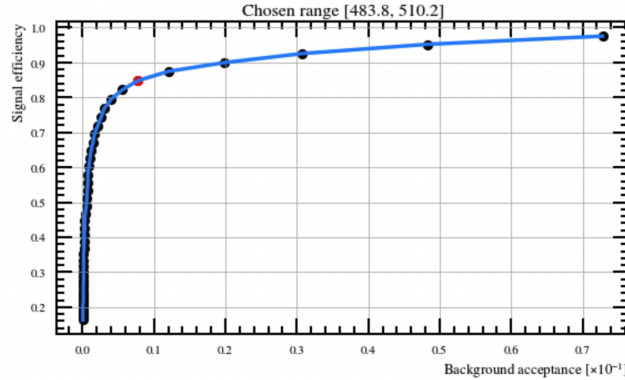
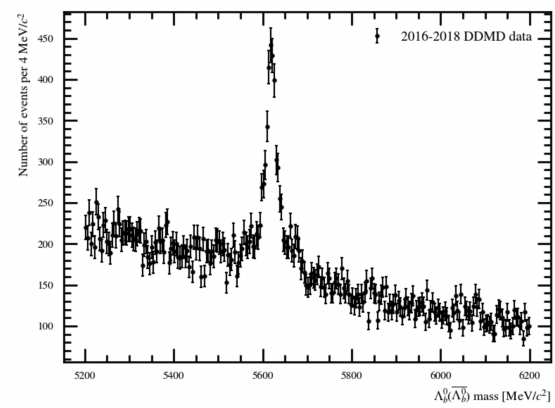
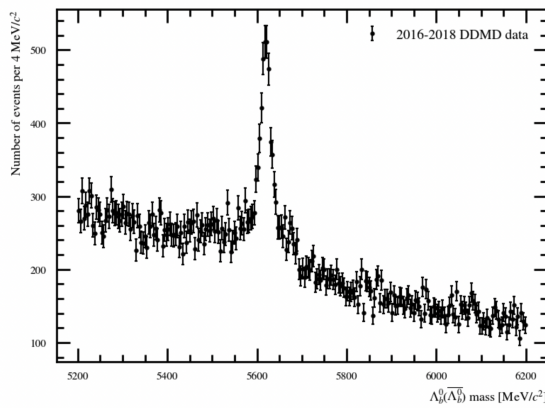


Figure 8: Signal efficiency and background acceptance values for each mass range. The mass range corresponding to the red data point is the one chosen for the cut veto.

Figure 9 and 10 show $\Lambda_b^0(\bar{\Lambda}_b^0)$ mass distributions before and after applying the veto. It is observed that while the cut preserves the shape of the signal, it effectively smooths the region just before the peak, where the K_s^0 contribution is expected to occur. It follows that the only remaining source of background is combinatorial.



4 Results

The signal yield is extracted through the sum of two Gaussian binned fits. A Gaussian probability density function is chosen to describe the core shape due to the main decay contribution, while the combination of two functions is used to take into account the broader contribution due to resolution effects.

The combinatorial background is fitted with an exponential function of the form ae^{-bx} , while the total fit is obtained by summing the signal and background fitting functions.

A selection is applied to the data to distinguish between Λ_b^0 and $\bar{\Lambda}_b^0$ particles, with different initial guesses calculated for each.

The signal fit initial parameters are derived from a preliminary fit on Monte Carlo simulated data, while those for the combinatorial background fit are obtained by applying the exponential function to the background regions only of the data distributions.

The same procedure is applied to determine the signal yield across all four samples and the binned data fits for each of them are presented in the plots shown in Figures 11 to 18.

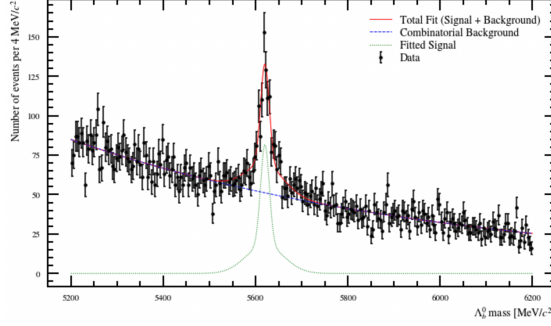


Figure 11: LLMD particle data.

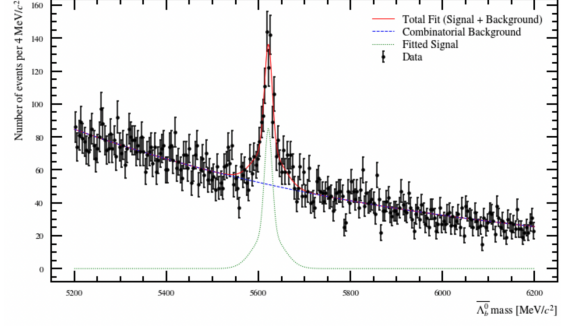


Figure 12: LLMD antiparticle data.

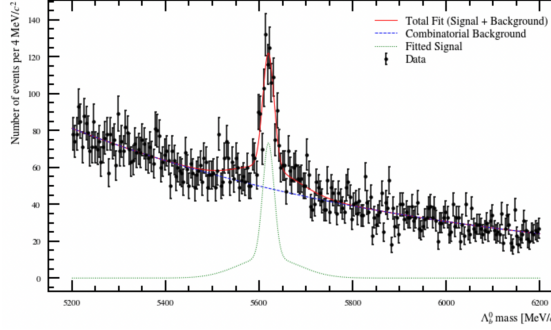


Figure 13: LLMU particle data.

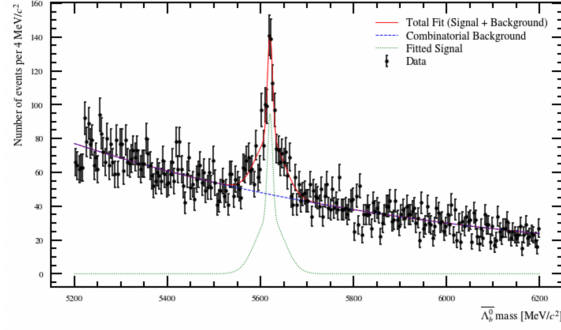


Figure 14: LLMU antiparticle data.

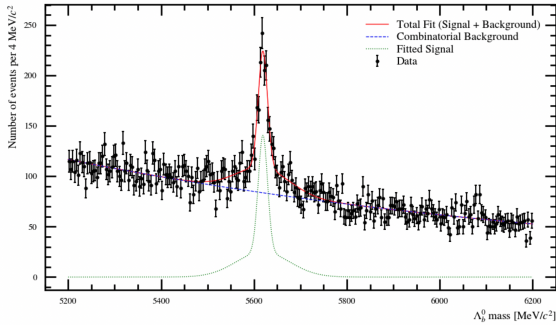


Figure 15: DDMD particle data.

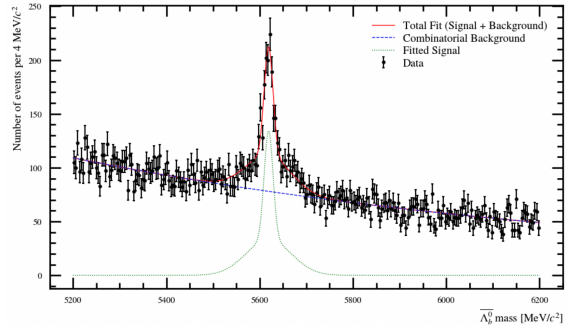


Figure 16: DDMD antiparticle data.

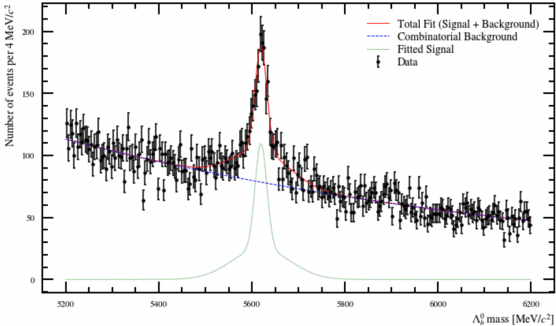


Figure 17: DDMU particle data.

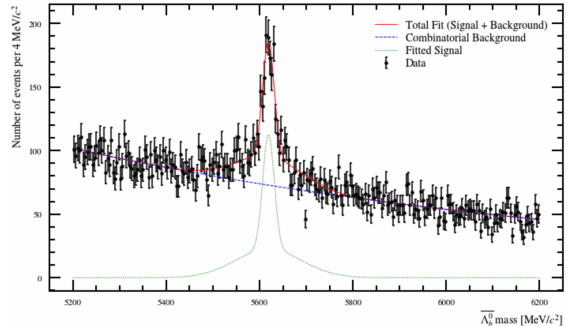


Figure 18: DDMU antiparticle data.

Furthermore, by combining the four data samples, the plots in Figures 19 and 20 are obtained.

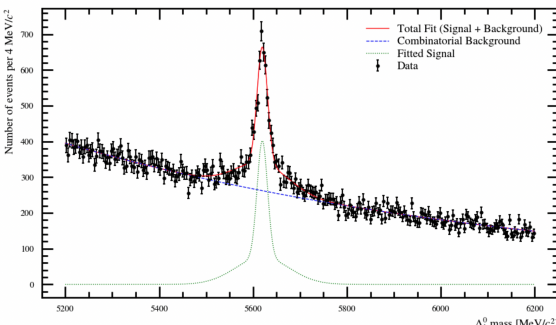


Figure 19: Particle selection on all DDMU, DDMD, LLMU, LLMD data.

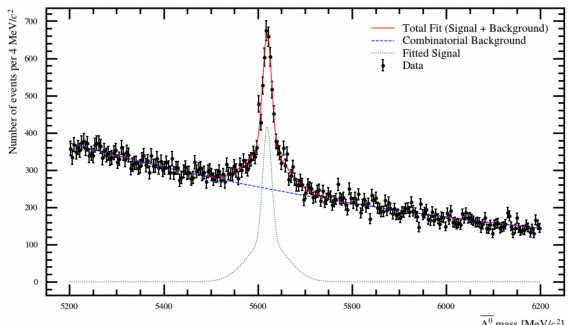


Figure 20: Antiparticle selection on all DDMU, DDMD, LLMU, LLMD data.

Two normalization parameters are used for the two Gaussian PDFs. The sum of these optimal values, divided by the bin width, provides the total signal yield for each plot, as shown in Table 4. Each value is displayed with its standard deviation.

The raw asymmetry ratio defined by the following equation:

$$A_{\text{raw}} = \frac{N_{\Lambda_b^0} - N_{\bar{\Lambda}_b^0}}{N_{\Lambda_b^0} + N_{\bar{\Lambda}_b^0}} \quad (3)$$

is calculated for each sample along with its associated uncertainty. This raw asymmetry includes contributions from different sources of asymmetry. The three main contributors to the raw asymmetry are: production asymmetry, decay asymmetry and detection asymmetry.

Production asymmetry arises from the proton-proton initial state from which more Λ_b^0 than $\bar{\Lambda}_b^0$ particles are expected to be produced [17].

Detection asymmetry stems from systematic effects in the detector, such as differences in efficiency when detecting particles versus antiparticles, variations in resolution or reconstruction biases. These latter effects are experimental artifacts rather than true physical asymmetries.

Lastly, the physical asymmetry in the decay process itself, which could potentially point to CP violation, is also a factor.

However, this ratio is considered an effective choice to investigate matter-antimatter asymmetry as systematic effects that similarly impact both particle and antiparticle measurements largely cancel out.

	Λ_b^0	$\bar{\Lambda}_b^0$	A^{raw}
LLMD	835 ± 94	760 ± 99	0.047 ± 0.086
LLMU	924 ± 105	842 ± 68	0.046 ± 0.069
DDMD	1620 ± 132	1612 ± 112	0.002 ± 0.053
DDMU	1635 ± 139	1690 ± 135	-0.016 ± 0.058
All samples	4983 ± 241	4696 ± 199	0.029 ± 0.032

Table 4: Signal yields and asymmetries for different data samples.

5 Discussion

The total fit of all data sets converges to both the signal and background effectively, allowing to extract the signal yields for both particle and antiparticle decays as shown in the Table 4. Initially, the signal was fitted using a Double-Sided Crystal Ball function [15], [18], where one side mirrors the other. The results of this attempt are presented in the Appendix. However, due to the complexity of the numerous parameters involved, this fit produced less accurate results, with uneven standard deviations between the Λ_b^0 and $\bar{\Lambda}_b^0$ number of events. Consequently, the sum of two Gaussian functions was deemed a better choice for the signal fit, as it consistently reproduces the signal peaks and event counts for the Λ_b^0 and $\bar{\Lambda}_b^0$ masses across all datasets, with mass distributions centered around the expected value of 5619 MeV.

By comparing the LL and DD plots, it is observed that the signal fit shapes are quite similar across the different data sets. A broader signal peak, and thus a larger standard deviation, was expected in the DD sample due to its poorer resolution compared to the LL sample. However, this effect is not observed, very likely because the post-bremsstrahlung-correction momentum resolution of the electrons is dominating the mass resolution of Λ^0 . In addition, the higher number of events in the DD sample compared to the LL sample indicates that more Λ^0 particles are detected decaying outside the VELO than within the region.

Moreover, by comparing MU and MD samples it is possible to investigate the possibility of a detection asymmetry. When the MU polarity is used to detect particles, positive decay products are bent upwards while negative particles are bent downwards. If a detection asymmetry is present, i.e. different detection efficiencies for particles moving in different directions, the bias will manifest in opposite ways when the magnet polarity is switched.

By comparing the number of events between the MD and MU samples in Table 4, no conclusive detection asymmetry can be observed in either the LL or DD samples, as the event counts are within one standard deviation of each other.

Finally, the total number of Λ_b^0 and $\bar{\Lambda}_b^0$ particles in the decay is presented in the combined 'all samples' category. As expected, the increased statistics in this category results in reduced uncertainties compared to the DD and LL samples. The raw asymmetry ratio, along with its propagated uncertainty, is shown in the last row and column of Table 4.

The latter value lies within its uncertainty range, indicating no evidence of a matter-antimatter asymmetry. This result is consistent with expectations, as the studied decay is described by a tree-level Feynman diagram, where, contrarily to higher-order diagrams, CP violation is not typically observed. It follows that the decay studied is a good candidate as a normalization channel for the $\Lambda_b^0 \rightarrow e^+e^-\Lambda^0$ decay, which is indeed described by an higher order Feynman diagram.

Finally, this analysis could be further improved by the use of unbinned fits. Indeed, signal yields and raw asymmetries can be determined for example with the use of unbinned maximum-likelihood fits to invariant mass distributions [17]. The maximum-likelihood fit is a statistical method used to model data and extract the most likely number of signal events while accounting for the background events. In this context, the fitting function might include parameters that describe both the signal and the background so that background due to particle misidentification is actually fitted along with the signal and not removed by veto from the data.

To conclude, analysis and understanding of systematic uncertainties would be beneficial to the solidity of the final results.

6 Conclusion

In this thesis, the $\Lambda_b^0 \rightarrow \Lambda^0 (\rightarrow p\pi^-) J/\psi (\rightarrow e^+e^-)$ decay is analysed in order to investigate the presence of CP violation. The raw asymmetry ratio, $A_{raw} = 0.029 \pm 0.032$, is measured on LHC Run 2 data collected between 2016 and 2018. The latter value leads to the conclusion that, in this study, no matter-antimatter asymmetry is observed. It follows that the decay analyzed can be considered a good candidate as a normalization channel for the $\Lambda_b^0 \rightarrow e^+e^-\Lambda^0$ decay.

Moreover, the comparison of MU and MD categories of data was aimed to investigate the presence of detector asymmetries. These effects were not observed since the signal yields in both LL and DD samples fall within one standard deviation of each other.

Finally, it is observed that Λ^0 particles decay more frequently outside the VELO region, leading to a higher number of events in the downstream track samples. However, it is still advantageous to include long track datasets to the analysis due to their superior resolution.

To conclude, further improvements such as the use of an unbinned fit to extract the signal yields would improve, not only the solidity of the results, but also enable comparisons with measurements reported in other papers. Finally, this analysis would also be improved by taking into account systematic uncertainties and by fitting the $B^0 \rightarrow J/\psi K_s^0$ background contribution along with the signal instead of applying a veto to the data.

7 References

- [1] The KTeV Collaboration, “Measurements of direct CP violation, CPT symmetry, and other parameters in the neutral kaon system,” vol. 67, no. 1, p. 012005, 2003.
- [2] The LHCb Collaboration, “Measurement of CP violation in $B^0 \rightarrow D^+D^-$ and $B_s^0 \rightarrow D_s^+D_s^-$ decays,” LHCb-PAPER-2024-027-003, Tech. Rep., 2024.
- [3] The LHCb Collaboration, “Observation of CP violation in charm decays,” *Physical review letters*, vol. 122, no. 21, p. 211803, 2019.
- [4] The LHCb Collaboration, “Test of lepton universality in beauty-quark decays,” *Nature Physics*, vol. 18, no. 3, pp. 277–282, 2022.
- [5] The Atlas Collaboration, “Observation of a new particle in the search for the Standard Model Higgs boson with the ATLAS detector at the LHC,” *Physics Letters B*, vol. 716, pp. 1–29, 2012.
- [6] The CMS Collaboration, “Observation of a new boson at a mass of 125 GeV with the CMS experiment at the LHC,” *Physics Letters B*, vol. 716, no. 1, pp. 30–61, 2012.
- [7] Wikimedia Commons, *Standard Model of Elementary Particles*, 2019. [Online]. Available: https://commons.wikimedia.org/wiki/File:Standard_Model_of_Elementary_Particles.svg.
- [8] D. Griffiths, *Introduction to elementary particles*. John Wiley & Sons, 2020.
- [9] The LHCb Collaboration, “The LHCb detector at the LHC,” vol. 3, no. 08, S08005, 2008.
- [10] The LHCb Collaboration, “Measurement of the track reconstruction efficiency at LHCb,” *Journal of Instrumentation*, vol. 10, no. 02, P02007, 2015.
- [11] R. Bruce, B. Salvant, T. Pieloni, *et al.*, “LHC Run 2: Results and challenges,” Tech. Rep., 2016.
- [12] The LHCb Collaboration, *LHCb Public Page*, <http://lhcb-public.web.cern.ch/>, 2023.
- [13] Particle Data Group, *Particle Data Group Live*, 2024. [Online]. Available: <https://pdglive.lbl.gov/Viewer.action>.
- [14] V. Dedu, “Branching Fraction Measurement of $\Lambda_b^0 \rightarrow J/\psi\Lambda$,” Master’s Thesis, University of Amsterdam, Amsterdam, Netherlands, Nov. 2020.
- [15] The LHCb Collaboration, “Differential branching fraction and angular analysis of $\Lambda_b^0 \rightarrow \Lambda\mu^+\mu^-$ decays,” *JHEP*, vol. 06, p. 115, 2015, [Erratum: JHEP 09, 145 (2018)]. DOI: [10.1007/JHEP06\(2015\)115](https://doi.org/10.1007/JHEP06(2015)115). arXiv: [1503.07138 \[hep-ex\]](https://arxiv.org/abs/1503.07138).
- [16] The LHCb Collaboration, “Measurement of lepton universality parameters in $B^+ \rightarrow K^+\ell^+\ell^-$ and $B^0 \rightarrow K^{*0}\ell^+\ell^-$ decays,” *Phys. Rev. D*, vol. 108, no. 3, p. 032002, 2023. DOI: [10.1103/PhysRevD.108.032002](https://doi.org/10.1103/PhysRevD.108.032002). arXiv: [2212.09153 \[hep-ex\]](https://arxiv.org/abs/2212.09153).
- [17] The LHCb Collaboration, “Observation of a $\Lambda_b^0 - \overline{\Lambda}_b^0$ production asymmetry in proton-proton collisions at $s = 7$ and 8 TeV,” *Journal of High Energy Physics*, vol. 2021, pp. 1–38, 2021.
- [18] Wikipedia contributors, *Crystal ball function*, 2024. [Online]. Available: https://en.wikipedia.org/wiki/Crystal_Ball_function.

8 Appendix

The uncertainty in the asymmetry ratio A is given by:

$$\Delta A = \sqrt{\left(\frac{2N_{\text{antiparticle}}}{(N_{\text{particle}} + N_{\text{antiparticle}})^2} \Delta N_{\text{particle}} \right)^2 + \left(\frac{-2N_{\text{particle}}}{(N_{\text{particle}} + N_{\text{antiparticle}})^2} \Delta N_{\text{antiparticle}} \right)^2}$$

where:

$$\frac{\partial A}{\partial N_{\text{particle}}} = \frac{2N_{\text{antiparticle}}}{(N_{\text{particle}} + N_{\text{antiparticle}})^2}$$

$$\frac{\partial A}{\partial N_{\text{antiparticle}}} = \frac{-2N_{\text{particle}}}{(N_{\text{particle}} + N_{\text{antiparticle}})^2}$$

$$\Delta N_{\text{particle}} = \sqrt{(\Delta n_1)^2 + (\Delta n_2)^2}$$

$$\Delta N_{\text{antiparticle}} = \sqrt{(\Delta n_{\text{anti}1})^2 + (\Delta n_{\text{anti}2})^2}$$

and:

N_{particle} = first + second normalization parameters in the particle data.

Δn_1 = the standard deviation of the first normalization parameter in the particle data.

Δn_2 = the standard deviation of the second normalization parameter in the particle data.

$N_{\text{antiparticle}}$ = first + second normalization parameters in the antiparticle data.

$\Delta n_{\text{anti}1}$ = the standard deviation of the first normalization parameter in the antiparticle data.

$\Delta n_{\text{anti}2}$ = the standard deviation of the second normalization parameter in the antiparticle data.

Initially, the signal was fitted using a Double-Sided Crystal Ball function [18] with one side being the mirror image of the other. The whole procedure is the same as the one described in Results section except the use of a different function to fit the signal. The binned data fits for each sample are displayed in the plots shown in Figures 21 to 30.

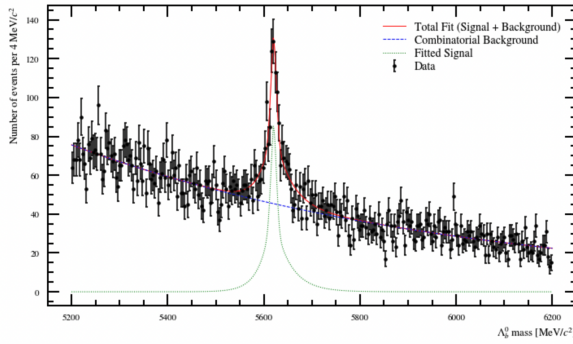


Figure 21: LLMD particle data.

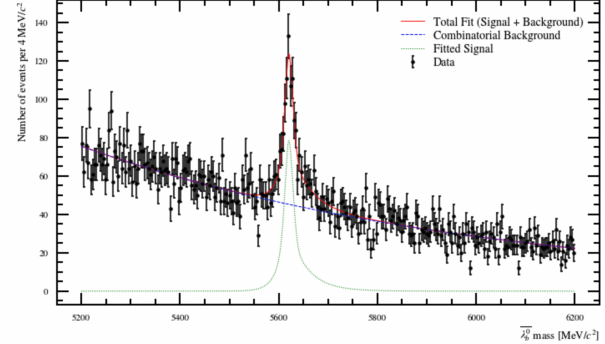


Figure 22: LLMD antiparticle data.

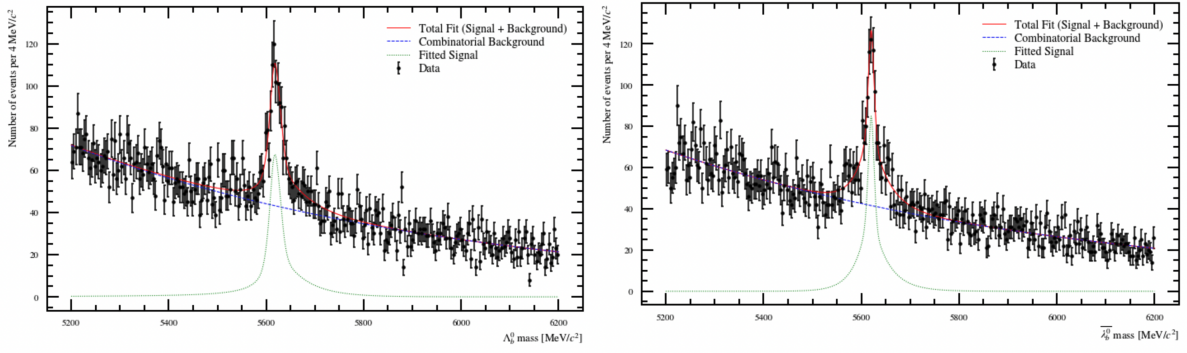


Figure 23: LLMU particle data.

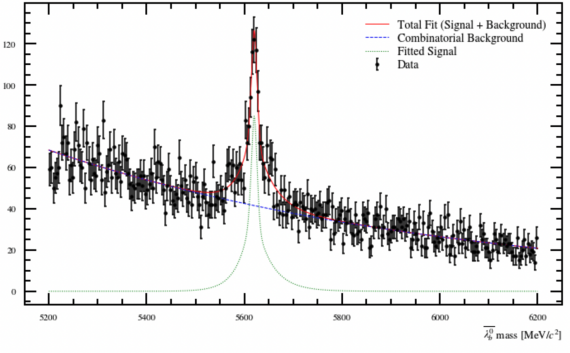


Figure 24: LLMU antiparticle data.

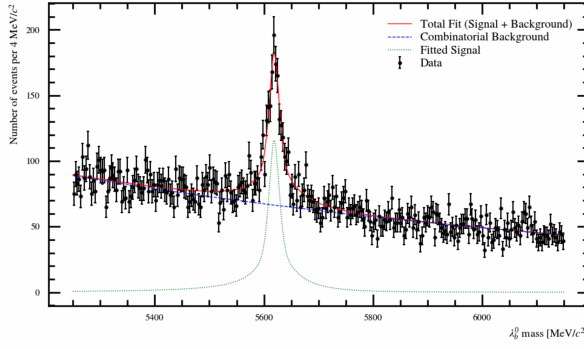


Figure 25: DDMD particle data.

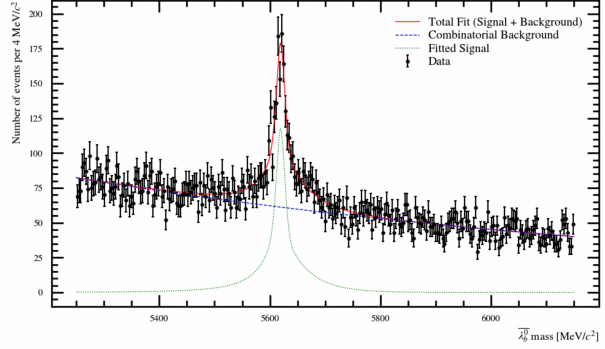


Figure 26: DDMD antiparticle data.

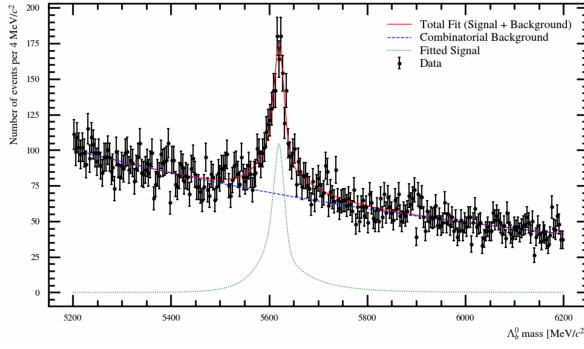


Figure 27: DDMU particle data.

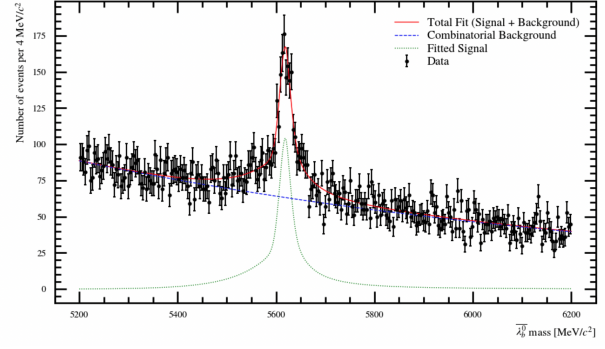


Figure 28: DDMU antiparticle data.

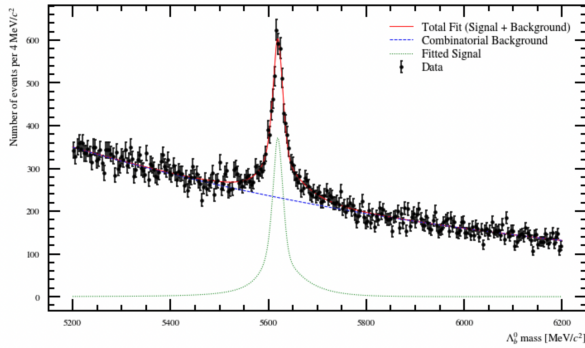


Figure 29: Particle selection on all DDMU, DDMD, LLMU, LLMD data.

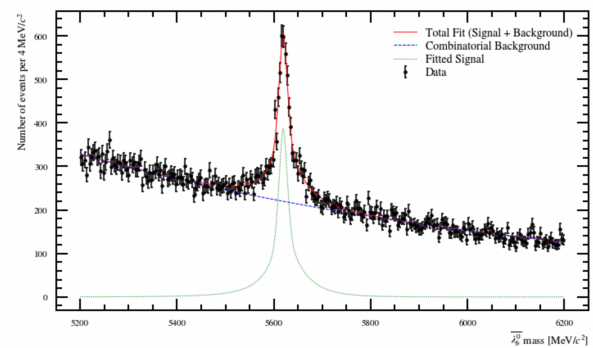


Figure 30: Antiparticle selection on all DDMU, DDMD, LLMU, LLMD data.

	Λ_b^0	$\overline{\Lambda}_b^0$	A^{raw}
LLMD	872 ± 123	831 ± 218	0.02 ± 0.15
LLMU	1059 ± 502	926 ± 130	0.07 ± 0.25
DDMD	1964 ± 1001	1874 ± 372	0.023 ± 0.273
DDMU	1900 ± 316	2249 ± 604	-0.08 ± 0.16
All samples	5388 ± 646	5342 ± 551	0.004 ± 0.079

Table 5: Signal yields and asymmetries for different data samples.